



**HAL**  
open science

## **Impact of topographic obstacles on the discharge distribution in open-channel bifurcations**

Emmanuel Jean Marie Mignot, C. Zeng, G. Dominguez, C.W. Li, N. Rivière, Pierre  
Henri Bazin

### ► **To cite this version:**

Emmanuel Jean Marie Mignot, C. Zeng, G. Dominguez, C.W. Li, N. Rivière, et al.. Impact of topographic obstacles on the discharge distribution in open-channel bifurcations. *Journal of Hydrology*, 2013, 494, p. 10 - p. 19. <10.1016/j.jhydrol.2013.04.023>. <hal-00840412>

**HAL Id: hal-00840412**

**<https://hal.science/hal-00840412v1>**

Submitted on 2 Jul 2013

**HAL** is a multi-disciplinary open access archive for the deposit and dissemination of scientific research documents, whether they are published or not. The documents may come from teaching and research institutions in France or abroad, or from public or private research centers.

L'archive ouverte pluridisciplinaire **HAL**, est destinée au dépôt et à la diffusion de documents scientifiques de niveau recherche, publiés ou non, émanant des établissements d'enseignement et de recherche français ou étrangers, des laboratoires publics ou privés.



HAL Authorization



29

## 30 **1. Introduction**

31 When an urban flood occurs, streets generally carry most of the flow from the upstream to downstream part  
32 of the city, especially when the area is densely urbanized (Mignot *et al.*, 2006). Flow in the streets is mostly  
33 1D with mean velocities parallel to the building façades. However, in crossroads several flows collide and/or  
34 separate and the flow pattern becomes complex (see Mignot *et al.*, 2008) especially when artificial  
35 topographies create additional flow structures such as wakes, recirculation zones and secondary flows. Bazin  
36 *et al.* (2012) have studied the impact of obstacles on a junction flow where two subcritical flows collide.  
37 They observed that this impact depends on the location of the obstacles and may i) strongly modify the local  
38 velocity distribution and ii) the extensions of a recirculation zone. Moreover, the authors observed that if an  
39 obstacle is located within a recirculation zone, the impact of the obstacle is strongly damped.

40 Within street bifurcations, with a single inflow separating into two outflows, artificial topographies can also  
41 affect the flow distribution reaching the downstream streets. The aim of the present paper is thus to  
42 investigate i) the impact of obstacles on the local flow characteristics in bifurcation flows and ii) the  
43 consequences of such modifications of the flow pattern on the modification of flow distribution to the  
44 downstream branches. The selected artificial topographies are squared emerging obstacles which would  
45 represent trees, bus-stop or any other impervious urban furniture located near crossroads.

46 The general pattern of a steady subcritical 3-branch bifurcation without obstacle is described by Neary *et al.*  
47 (1999). A three-dimensional recirculating region develops in the lateral branch and secondary flows appear in  
48 both outlets. The principal challenge in such separating flow lies in the prediction of flow distribution from  
49 the incoming towards both outgoing flows. A review of analytical models developed to access such  
50 prediction is given by Rivière *et al.* (2007). The models are based on the momentum conservation law (see  
51 for instance Ramamurthy *et al.*, 1990), but Rivière *et al.* (2006) showed that this balance alone does not  
52 permit to calculate the flow distribution, and that additional equations must be introduced. These authors  
53 proposed an improved relationship based on i) the momentum conservation law from Ramamurthy *et al.*  
54 (1990), ii) suitable stage-discharge relationships for the downstream controls in the outflow channels and iii)  
55 an empirical correlation obtained through experimental data. This approach proved to accurately predict the  
56 flow distribution in three-branch bifurcations in ideal conditions: 90° angle, smooth walls and identical  
57 horizontal rectangular sections in each branch. Riviere *et al.* (2011) then generalized the results to 4-branch  
58 intersections.

59 Nevertheless, when singularities are introduced near or in the bifurcation, the flow pattern can be strongly  
60 affected and this analytical model obviously does not apply. The question raised by the present paper is to  
61 what extent an introduction of single or pairs of obstacles in the vicinity of the intersection affects the  
62 discharge distribution. Nine configurations of simplified square-shaped obstacles of typical size equal to 1/6  
63 of the channel width are tested here. Their impact on the flow pattern and the downstream flow rates is  
64 analyzed for 14 flow configurations divided in 3 series.

65 For practical reasons, velocity field for all flow configurations with all obstacles could not be measured  
66 experimentally. The selected approach is rather based on a mix of experimental measurements and 3D  
67 calculations. After verification of their accuracy, these calculations are considered reliable enough to support  
68 the experimental investigation. In the first and second sections we describe the experimental and numerical  
69 methodologies respectively along with the selected flow and obstacle configurations. In a third section, we  
70 describe the impact of the obstacles on the flow pattern and discharge distribution and finally discuss the  
71 impact of the base flow (before introducing obstacles) characteristics on such results.

72

## 73 **2. Experimental methodology**

### 74 **2.1 Experimental set-up**

75 The experiments were performed in the channel intersection facility at the Laboratoire de Mécanique des  
76 Fluides et d'Acoustique (LMFA) at the University of Lyon (Insa-Lyon, France). The facility consists of three  
77 horizontal glass channels 2m long and  $b=0.3\text{m}$  wide each. The channels intersect at  $90^\circ$  with one upstream  
78 branch (with the flow rate  $Q_u$ ), one downstream branch (flow rate  $Q_d$ ) aligned with the upstream one and one  
79 lateral branch (flow rate  $Q_b$ ). The upstream branch is connected to a large upstream storage tank where the  
80 flow is straightened and stabilized by passing through a honeycomb. The flow separates in the bifurcation  
81 and is finally collected by the downstream and lateral tanks. The lateral tank is connected to the downstream  
82 tank and the lateral discharge  $Q_b$  is measured using an electromagnetic flow-meter (see Figure 1). When  
83 pumped from the downstream tank to the upstream tank, the upstream flow-rate  $Q_u$  is measured using a  
84 second electromagnetic flow-meter. In order to control the flow conditions, PVC channels (length 60 cm)  
85 fitted with sharp crested weirs are added to the ends of the two exit channels so that  $L_d=L_b=2.6\text{m}$  while  
86  $L_u=2\text{m}$ . A more detailed description of the experimental set-up can be found in (Rivière *et al.*, 2011).

87 For each flow configuration, the three boundary conditions to be set are: the upstream flow rate  $Q_u$  and the  
88 height of the sharp crest weirs  $C_d$  (for the downstream branch) and  $C_b$  (for the lateral branch). The stage

89 discharge relationship ( $h_n, C_n, Q_n$ ,  $n=b$  or  $d$ ) is calibrated experimentally for each weir:  $h_b$  and  $h_d$  are measured  
90 using a digital point gauge at a length equal to 2 channel width upstream from the weirs. Similarly, the  
91 upstream water depth  $h_u$  used to characterize the upstream velocity and Froude number is measured one  
92 channel width upstream from the entry section of the bifurcation (see Figure 1). A point gauge is used to  
93 measure backwater curves in the main and the branch channel for most flow configurations.

94 Upstream water depth  $h_u$  ranges from 25 to 71 mm and discharge  $Q_u$  from 1.6 to 7.0 L/s. The corresponding  
95 Reynolds number ranges between 18000 and 65000 and the corresponding Froude number from 0.23 to 0.69.  
96 Moreover, the roughness height  $k_s$  was measured using a roughness meter which revealed that the maximum  
97 roughness is smaller than 1  $\mu\text{m}$  and the average roughness smaller than 0.1  $\mu\text{m}$ . Given the hydraulic  
98 diameter, ranging from  $D_h = 0.08\text{m}$  to 0.2m, the maximum relative roughness  $k_s/D_h$  is estimated to about  $10^{-5}$ ,  
99 corresponding to a hydraulically smooth regime in the Moody diagram.

## 100 2.2 Dimensional analysis and flow series

101 Dimensional analysis is applied to the present flow configuration. The 13 variables to be included in the  
102 dimensional analysis of discharge distribution law without obstacle are the channel width  $b$  and roughness  $k_s$ ,  
103 the acceleration due to gravity  $g$ , the three flow rates and associated water depths  $Q_u$  and  $h_u$ ,  $Q_b$  and  $h_b$ ,  $Q_d$   
104 and  $h_d$ , the two weir crest heights  $C_d$  and  $C_b$  and finally the fluid density  $\rho$  and dynamic viscosity  $\mu$ .

105 5 available straightforward equations are:

106 - the mass conservation, which yields  $Q_u = Q_b + Q_d$ , permitting to remove the  $Q_d$  parameter.

107 - both calibrated stage discharge relationships ( $h_b, C_b, Q_b$ ) and ( $h_d, C_d, Q_d$ ), permitting to remove the  $C_b$  and  $C_d$   
108 parameters.

109 - the momentum balance in the bifurcation along the main flow axis ( $x$ ) as proposed by Ramamurthy *et al.*  
110 (1990) relating ( $h_u, h_d, Q_b$ ) and thus permitting to remove the  $h_d$  parameter

111 - the empirical discharge distribution law proposed by Riviere *et al.* (2007) in their equation 2b which links  
112 the discharge distribution  $Q_b/Q_u$  with  $h_b$  through three parameters:  $Q_d/(b \cdot g \cdot h_d^{3/2})$ ,  $h_d/b$  and  $h_b/h_d$ , thus  
113 permitting to remove  $h_b$ .

114 The 8 remaining variables are then  $b, g, Q_b, Q_u, h_u, k_s, \rho$  and  $\mu$ , including three scales, *i.e.* a time scale  $b^3/Q_u$ , a  
115 length scale  $b$  and a mass scale  $\rho b^3$ .

116 Among the 5 final dimensionless parameters that rule the flow, two of them are discarded in this study. First  
117 one is the Reynolds number  $Re = 4\rho Q_u / [\mu(b + 2h_u)]$ , as its values are reasonably high (see section 2.1) to ensure  
118 fully turbulent flows. Second one is the dimensionless roughness height  $k_s/D_h$ , with  $D_h$  the hydraulic

119 diameter. As the flow regime is hydraulically smooth (see section 2.1), effect of the roughness parameter is  
120 not considered hereafter.

121 The 3 final dimensionless parameters considered herein are then:

122 - the upstream Froude number  $F_u = Q_u / [b \cdot h_u \cdot (g \cdot h_u)^{0.5}]$

123 - the discharge distribution parameter  $R_q = Q_b / Q_u$

124 - the normalized upstream water depth  $h_u / b$

125 These three parameters govern the flow distribution in the 3-branch bifurcation without obstacle. In the  
126 sequel we investigate the impact of introducing obstacles in flows with varying value of each of these three  
127 parameters at a time. The flow configurations before introducing any obstacle are labeled “0” or “base” flow.  
128 Consequently, three series (S1, S2 and S3) of base flow configurations are considered in Table 1: S1 with  
129 varying  $F_{u0}$  and fixed  $R_{q0}$  and  $h_{u0}/b$ , S2 with varying  $R_{q0}$  and fixed  $h_{u0}/b$  and  $F_{u0}$  and S3 with varying  $h_{u0}/b$  and  
130 fixed  $R_{q0}$  and  $F_{u0}$ .

### 131 **2.3 Obstacle configurations**

132 For each base flow configuration (without obstacle) from Table 1, each obstacle is introduced one after the  
133 other near the bifurcation as shown on Figure 2. 10 obstacle configurations are considered for each flow:  
134 configuration labeled 0 is without obstacle (base); configurations labeled 1 to 7 comprise one obstacle;  
135 configurations labeled 8 and 9 comprise two obstacles (obstacles 2 + 4 for configuration 8 and 2 + 6 for  
136 configuration 9). The obstacles are square-shaped (section is 5x5cm), impervious, emerging (height is 20  
137 cm), smooth blocks. They are led on the bottom and heavy enough to remain stable in the flow. They are  
138 located at a distance of 4 cm from the closest wall and junction section (as for obstacle 5 on Figure 2) except  
139 for obstacle 7 which is located at the center of the bifurcation.

### 140 **2.4 Methodology**

141 For each flow from Table 1:

142 - we adjusted the boundary conditions ( $C_d$ ,  $C_b$ ,  $Q_u$ ) to obtain the desired base flow configuration without  
143 obstacle (labeled “0”).

144 - we measured the corresponding discharges  $Q_{b0}$ ,  $Q_{d0}$  without obstacle as shown on Figure 1.

145 - we introduced each of the 9 obstacles one after the other without changing the boundary conditions ( $C_d$ ,  $C_b$ ,  
146  $Q_u$ ) and in each case, we measured the downstream discharges  $Q_{bi}$ ,  $Q_{di}$ , with “i” the obstacle number.

147 - we computed the indicator of discharge distribution modification corresponding to the introduction of each  
148 obstacle  $\Delta R_q = 100 \cdot (R_{qi} - R_{q0}) = 100 \cdot (Q_{bi} - Q_{b0}) / Q_u$ ,  $i = 1 \dots 9$ .

149 This methodology thus permits to investigate i) the impact of each obstacle on the discharge distribution for  
150 each flow from Table 1 and ii) the evolution of such impact with the evolution of the characteristics of the  
151 base flow ( $F_{u0}$ ,  $R_{q0}$  and  $h_{u0}/b$ ).

## 152 **2.5 Velocity fields measured through PIV**

153 In addition to discharge measurements, the horizontal velocity field is measured using PIV at a selected  
154 elevation  $z=3\text{cm}$  for the flow configuration in bold in Table 1. This configuration is the slowest flow from the  
155 list and thus leads to the better measurement accuracy. Moreover, no PIV measurement could be performed  
156 using obstacle 7 as a large portion of the intersection would be in the shade of the obstacle.

157 Polyamid particles (50  $\mu\text{m}$  diameter) are added to the water which re-circulates in our closed loop. A  
158 generator emitting white light through a slot is used to create a plane, 5 mm thick, light sheet at the  
159 measurement elevation ( $z=3\text{cm}$ ) in the channel junction and the branch channel. A 1280x1920 pixel  
160 progressive CCD-camera with 8 mm opening objective and 25ms time-exposure connected to a PC computer  
161 through a Firewire acquisition card is located above the free surface at an elevation of about 1.1 m. Inserting  
162 the whole set-up in the dark finally permits to record the particle motion at the lightened elevation at a fixed  
163 frame-rate of 30Hz during 133s. 4000 images are then recorded. The dimension of the measurement region is  
164 350x500 mm with a horizontal resolution of 0.5 mm per pixel with 256 grey-levels. The commercial  
165 software Davis (from Lavision) permits to correct the optical distortions, to subtract the background and to  
166 compute each of the 4000 velocity fields over a 15x15 mm grid, that is about 20 points per channel section.  
167 The data is then averaged over the whole recording time to obtain the time-averaged velocity fields shown in  
168 Figure 5.

169

## 170 **3. Numerical Simulation**

### 171 **3.1 Numerical method**

172 In the numerical model, the 3D Unsteady Reynolds Averaged Navier-Stokes (URANS) equations for the  
173 conservation of mass and momentum of fluid are solved. The Reynolds stresses are represented by the eddy  
174 viscosity concept and the Spalart-Allmaras (SA) model is used for the turbulence closure. The  $\sigma$ -coordinate  
175 transformation is used to map the irregular domain with variable free-surface and bottom topography to a  
176 rectangular prism. A split-operator finite difference method with non-uniform rectilinear grid is employed to

177 solve the governing equations. In each time interval, the equations are split into three steps: advection,  
178 diffusion and pressure propagation. In the advection step a characteristics-based scheme is used. In the  
179 diffusion step a centered difference scheme is used. In the pressure propagation step a Poisson equation is  
180 derived and solved by a stable and robust conjugate gradient method CGSTAB. A comparison of the velocity  
181 profiles in a bifurcation flow (without obstacle, measured by Barkdoll, 1997) computed by Li and Zeng  
182 (2009) using the present SA model and by Neary *et al.* (1999) using a  $k-\omega$  model reveals that the two sets of  
183 results are quite similar. Further details of the present model can be found in (Lin and Li, 2002) and  
184 applications of the numerical model to flow division problems in open channels were performed by Li and  
185 Zeng (2010).

186 For the present application, the boundary conditions used are as follows. At the channel inlet the discharge  
187  $Q_u$  is prescribed, the velocity profile is assumed uniform and the eddy viscosity profile is specified by using  
188 the mixing length model, the surface elevation gradient is set to zero and the pressure is assumed hydrostatic.  
189 At both channel outlets the water depth and the discharge are related by the experimental weir equations  
190  $(h_b, C_b, Q_b)$  and  $(h_d, C_d, Q_d)$  and the streamwise gradients of the pressure and of the three velocity components  
191 are set to zero. At the free surface, the pressure is assumed atmospheric (zero relative pressure), the gradients  
192 of the velocity components are set to zero and the free surface elevation is tracked by solving the kinematic  
193 equation. At solid boundaries (channel walls and obstacles) the normal gradients of pressure and velocity are  
194 set to zero, and the velocity components along the boundaries are specified by the standard wall function,  
195 considering smooth walls. All 14 flow cases given in Table 1 with the base (no obstacle) and 9 obstacle  
196 configurations are replicated in the numerical simulation. The grid system used is rectilinear and non-  
197 uniform, with the finest grid size used near solid boundaries. The total number of grid points is 182160.

### 198 **3.2 Validation of numerical method**

199 A comparison between the computed and measured outlet discharges for all flow configurations using each  
200 obstacle configuration is given in Figure 3. The results are accurate, the difference between the computed and  
201 corresponding measured downstream outlet discharges is generally within 5% of the inlet discharge. This  
202 gives confidence regarding the model capacity to predict the flow distribution. Moreover, Figure 4 presents a  
203 comparison of measured and computed water depth evolution along the main channel for the reference flow  
204 configuration (see \* in Table 1) without obstacle and with obstacle 7. The results are generally satisfactory  
205 and within 5% difference of the water depth. Nevertheless, the computed outlet water depth without obstacle  
206 is slightly higher than the measurements. Indeed, in the present case the downstream discharge is slightly  
207 overestimated by the calculation and thus, using the downstream stage-discharge relationship, the

208 corresponding water depth is also overestimated. Overall, the tendency remains similar. Regarding the case  
209 with obstacle 7, the discharge distribution is fairly estimated and thus also the downstream backwater curve,  
210 but the computed head loss in the intersection is slightly lower than the measured one. Moreover, grid  
211 refinement study was carried out. The number of grid points used in the fine grid system was four times of  
212 that used in the original grid system. The corresponding computed backwater curves are shown in Fig. 4. The  
213 maximum difference between the two set of results is approximately 2%. The discharge distribution and the  
214 velocity profiles at various locations were also compared in Table 2. The difference in the discharge  
215 distribution is within 3%. Finally, the sensitivity of the solution to the inlet velocity profile was also studied:  
216 the replacement of the uniform velocity profile by a logarithmic profile only marginally affects the solution  
217 (see Figure 4), showing that the length of the upstream channel is sufficiently long to eliminate inlet effects.

218 Finally, a comparison of five measured and computed velocity field in the intersection region for the bold  
219 flow from Table 1 is included in Figure 5: without obstacle ( $O_0$ ) and with obstacles 1, 2, 4, 5. As computed  
220 data results from unsteady numerical simulations, a time-averaging process was applied to the computed data  
221 for a better comparison with the time-averaged measured data. The magnitude of the velocity is generally  
222 satisfactorily predicted, except for the accelerated upstream flow near the right bank for obstacle 2. To  
223 conclude, the numerical model is considered as validated. In the sequel, the analysis of the impact of  
224 obstacles on the flow pattern is performed both from experimental and numerical data.

225

## 226 **4. Results**

227 Measured and computed velocities (Figure 5) and depths (Figure 6) reveal that the obstacles cause pile up of  
228 water immediate upstream and generate downstream wake regions with recirculating flows, leading to flow  
229 and streamline deflections. In the first subsection the impact of the obstacles on a selected flow (“PIV  
230 measured flow” in Table 1) is analyzed and in the three following sub-sections, the influence of the base flow  
231 characteristics from each serie in Table 1 on the obstacle impact is discussed.

### 232 **4.1 Impact of the obstacles on the flow pattern and discharge distribution on a selected flow**

233 Considering the PIV measured base flow (bold in Table 1) and using Figures 5, 6, 7 and 8, it is observed that:

234 - Without obstacle, the main flow is separated into two parts by the plane interface. The velocity along  $x$  axis  
235 thus decreases within the intersection. Maximum velocity along  $y$  axis is encountered in the lateral branch  
236 along the left bank wall while a recirculation zone is observed along the right bank wall. The water depth

237 increases from the junction to the downstream branch while it decreases toward the lateral branch (see Figure  
238 6). This behavior is in fair agreement with flow description in the literature by Neary *et al.* (1999)

239 - Introducing obstacle 1 strongly accelerates the right part of the upstream flow ( $-150\text{mm} < y < -300\text{mm}$ ) in the  
240 section. Due to the increased momentum (inertia), the capacity of the flow to rotate towards the lateral branch  
241 is strongly reduced and the discharge in the lateral branch decreases ( $\Delta R_q < 0$  in Figure 7).

242 - Introducing obstacle 2 deflects a large portion of the upstream flow towards the opposite wall ( $y=0$ ) where  
243 it is accelerated. This reduces the flow entering the lateral branch ( $\Delta R_q < 0$ ) and causes a reduction in the water  
244 depth in the lateral branch.

245 - Introducing obstacle 3 does not affect the flow pattern nor the discharge distribution as it is located within  
246 the very slow recirculation zone (dead zone, see Figure 8).

247 - Introducing obstacle 4 dramatically limits the section of the mean flow in the lateral branch near the  
248 downstream wall ( $0.2\text{m} < x < 0.3\text{m}$  and  $-0.6\text{m} < y < -0.3\text{m}$ ). The branch discharge is thus reduced ( $\Delta R_q < 0$ ) and the  
249 flow pattern within the branch is also strongly modified.

250 - Introducing obstacles 5 and 6 limits the flow section in the downstream branch, causes pile-up of the  
251 junction water depth, which tends to increase the discharge in the lateral branch ( $\Delta R_q > 0$ ).

252 - Introducing obstacle 7 tends to accelerate the flow along  $x$  axis within the junction on both sides of the  
253 obstacle (see Figure 8). The part of inflow deflected to the left bank ( $y > -150\text{mm}$ ) reaches the downstream  
254 branch while the part deflected to the right bank is itself separated in two parts, each part reaching one outlet  
255 channel. The deflection towards right side enhances the flow reaching the lateral branch and thus leads to  
256  $\Delta R_q > 0$ .

257 To conclude, it appears that both upstream obstacles (1 - 2) lead to  $\Delta R_q < 0$  while both downstream obstacles  
258 (5 - 6) lead to  $\Delta R_q > 0$ . Oppositely, impact of both lateral obstacles (3 - 4) on  $\Delta R_q$  differs. Moreover, Figure 7  
259 reveals that the impact of introducing obstacle configurations 8 (resp. 9) is about the sum of the impacts of  
260 the constituting obstacles, that is of obstacles 2+4 (resp. 2+6).

## 261 **4.2 Impact of the inflow Froude number: $F_{u0}$ (Serie 1)**

262 Figure 7 reveals that the sign (positive or negative) of  $\Delta R_q$  for a given obstacle does not change with varying  
263 Froude number of the base flow: none of the curves crosses the  $\Delta R_q = 0$  axis. It appears that as the Froude  
264 number of the base flow increases, the impact of each obstacle raises:  $|\Delta R_q|$  increases. Indeed, the Froude

265 number is the square root of the ratio between inertia force and gravity force. So, as the resistance force (drag  
266 force) produced by the flow on an obstacle is proportional to the square of the flow velocity, the increase in  
267 flow inertia leads to an increased resisting force on the obstacles. In return, as the Froude number of the flow  
268 increases, the pile-up at the stagnation point in front of the obstacle and the intensity of the wake increase.  
269 Both processes affect the flow pattern and thus the obstacle impact is enhanced. Moreover, Figure 7 reveals  
270 that for the flows studied in Serie 1, magnitude of discharge distribution modification ranges between less  
271 than 5% for the low Froude number configurations to a maximum of 10% for the highest Froude number.  
272 Modifications are then limited for all flow and obstacle configurations.

### 273 **4.3 Impact of the base discharge distribution: $R_{q0}$ Series 2**

274 Figures 8 and 9 show the impact of introducing obstacles in flows which base discharge distribution  $R_{q0}$   
275 (without obstacle) varies between 0.2 and 0.8. Experimentally, increasing  $R_{q0}$  with constant  $F_{u0}$  and  $h_{u0}/b$  is  
276 obtained by keeping the same upstream discharge  $Q_u$  and water depth  $h_u$  and by increasing (resp. decreasing)  
277 the weir crest height in the downstream channel  $C_d$  (resp. branch  $C_b$ ). Thus for constant upstream flow  
278 conditions, varying  $R_{q0}$  affects (see Figure 8): i) the location of the interface-plane which separates the  
279 upstream flow into a left portion reaching the downstream branch and a right portion reaching the lateral  
280 branch, ii) the width of the recirculation region in the branch and iii) the tendency of the downstream flow to  
281 detach from the left bank ( $y=0$ ) and to initiate a recirculation zone in the downstream branch. Assuming a 2D  
282 flow, the interface between both inflows starts in the upstream branch and ends at the downstream corner of  
283 the junction. For  $R_{q0}=0.5$ , the upstream limit of the interface plane is located at the centerline of the upstream  
284 branch ( $x<0$ ,  $y=-b/2$ ), while for  $R_{q0}<0.5$  this plane starts at  $y<-b/2$  and for  $R_{q0}>0.5$ , it starts at  $y>-b/2$ .  
285 Tendencies of  $\Delta R_q$  for increasing  $R_{q0}$  with the nine obstacles are summarized in Table 3. The relative location  
286 of this interface and each obstacle permits to explain most results:

287 - For low  $R_{q0}$ , the interface is located near the lateral branch side and thus far from **obstacle 1**. As obstacle 1  
288 then tends to accelerate the flow, its rotation capacity towards the lateral branch decreases:  $\Delta R_q < 0$  (see  
289 section 4.1). For increasing  $R_{q0}$ , the interface starts closer to obstacle 1 and part of upstream flow deflected to  
290 the right side of the obstacle passes to the right side of the interface of the base flow and finally reaches the  
291 lateral branch. Consequently, the  $\Delta R_q < 0$  tendency described above decreases as  $R_{q0}$  increases.

292 - Oppositely, as  $R_{q0}$  increases the interface plane goes away from **obstacle 2** and the discharge distribution  
293 becomes less influenced by the obstacle:  $|\Delta R_q|$  decreases. It should be noted that for very low  $R_{q0}$ , the base  
294 flow interface plane becomes located very close to the right bank of the inflow and thus the part of the flow

295 deflected by obstacle 2 to the right side of the inflow leads to an increase of  $\Delta R_q$  compared to slightly higher  
296  $R_{q0}$  (see Figure 9).

297 - **Obstacle 4** is located in the major flow zone of the branch channel. Its blockage effect increases with the  
298 lateral outflow discharge, that is as  $R_{q0}$  increases.

299 - **Obstacles 5 and 6** tend to block the flow in the downstream channel and thus to increase the branch  
300 discharge (see section 4.1). However, for increasing  $R_{q0}$  values, the discharge in the downstream channel  
301 decreases and thus also the velocity at this section. Corresponding pile-up and adverse pressure gradient thus  
302 decreases. Consequently, introducing obstacles 5 and 6 always leads to  $\Delta R_q > 0$  but this impact decreases as  
303  $R_{q0}$  increases.

304 - For  $R_{q0}$  lower or close to 0.5, **obstacles 7** tends to deflect most of the right part of upstream flow towards  
305 the branch side leading to  $\Delta R_q > 0$  (see section 4.1 and Figure 8). At the same time, the acceleration in the  
306 downstream channel suppresses the flow separation at the left bank. However, for  $R_{q0}$  much larger than 0.5,  
307 part of the flow which reached the lateral branch when no obstacle was included is now deflected by obstacle  
308 7 towards the left wall ( $y=0$ ) and finally reaches the downstream channel. As a consequence, for very high  
309  $R_{q0}$ , obstacle 7 benefits the downstream channel and  $\Delta R_q < 0$ .

310 - **Obstacle configurations 8 and 9** follow the same trend as their constitutive obstacles (2+4 for obstacle 8  
311 and 2+6 for obstacle 9).

312 - The impact of **obstacle 3** is related to the recirculation width in the lateral branch. According to Figure 8, as  
313  $R_{q0}$  increases, the width of the recirculation region in the lateral branch decreases and thus **obstacle 3** tends to  
314 pass from the recirculation zone to the main flow. As a consequence, for high  $R_{q0}$ , obstacle 3 tends to block  
315 off part of the lateral branch flow (increasing the water depth and creating an adverse pressure gradient),  
316 leading to  $\Delta R_q < 0$ .

#### 317 **4.4 Impact of the normalized water depth: $h_{u0}/b$ (Serie 3)**

318 Figures 10 and 11 show the influence of the upstream water depth of the base flow  $h_{u0}$  on the impact of each  
319 obstacle. First, it appears that the effect of water depth on the change in flow distribution is negligible except  
320 for the 3 configurations involving obstacle 2 (configurations 2, 8 and 9) where it still remains limited. For  
321 these configurations, as the base water depth increases (with similar Froude number and discharge  
322 distribution), the discharge in the branch is reduced:  $\Delta R_q < 0$  decreases until a minimum value for  $h_{u0}/b \sim 0.18$   
323 and then increases again for higher water depths. Numerical results in Figure 10 show that varying the water

324 depth  $h_{u0}$  affects the wakes generated downstream from obstacles 1 and 2, even though all our experiments  
325 belong to the “vortex street” flow type, when following Chen & Jirka (1995) approach. Indeed, the wake  
326 parameter  $S=f.a/(4h_u)$  ranges from 0.003 to 0.013 (*i.e.*  $S<0.2$ ), with  $a=0.05\text{m}$  the obstacle width and  $f$  the  
327 Darcy-Weisbach coefficient ranging from 0.02 to 0.027 considering smooth walls in our experiments. For  
328 obstacle 1, the wake modification hardly affects the discharge distribution (see Figure 11) as the obstacle is  
329 located far from the separation streamline. Oppositely, for obstacle 2, the wake modification appears to be  
330 responsible for the modification in discharge distribution for configurations 2, 8 and 9. This information  
331 revealed by the numerical results proves the interest of coupling experimental and numerical data for the  
332 analysis.

333

## 334 **5. Discussion and Conclusion**

335 The aim of the present paper was to investigate how the flow is affected by obstacles located in a 3-branch  
336 bifurcation with specific attention towards the impact on the discharge distribution to the downstream  
337 branches. Two types of measurements were undergone: i) discharge distribution measurements for 14 flows  
338 belonging to three series in which only one main parameter of the flow was varying at a time and in which 9  
339 obstacles were introduced one after the other; and ii) horizontal velocity field for one selected flow with most  
340 obstacle configurations using PIV techniques. In parallel all flows with all obstacle cases were computed  
341 using a CFD approach. Combination of both experimental and numerical approaches permitted to explain the  
342 outlet discharge modifications induced by obstacles by analyzing the changes in the flow pattern. The  
343 following conclusions can be outlined:

344 - The computation results of the numerical model in terms of outlet discharges and flow field are in  
345 fair agreement with measurements and thus this CFD model represents a suitable predictive tool to further  
346 study localized urban flooding configurations where the flow is strongly complex and 3D.

347 - The impact of an impervious obstacle on the discharge distribution in a subcritical 3-branch  
348 bifurcation flow is strongly dependent on the location of the obstacle with regards to the intersection.  
349 Obstacles located within the upstream branch increase the streamwise flow velocity and thus tend to reduce  
350 the lateral and increase the downstream discharge ( $Rq_0$  decreases up to 12%). Oppositely obstacles located  
351 within the downstream branch tend to block off the flow in this branch and to reduce the corresponding  
352 discharge while increasing the lateral discharge ( $Rq_0$  increases up to 3%). Finally for obstacles located within  
353 the lateral branch, their impact depends on the side of the channel in which they are introduced: i) towards  
354 the downstream wall of the lateral branch, they tend to block off the lateral flow and thus promote the

355 downstream and reduce the lateral discharge ( $Rq_0$  decreases up to 4.5%); ii) towards the upstream wall, the  
356 obstacle is usually located within the recirculation zone where it has no impact but as the width of this zone  
357 reduces, the obstacle can block off part of the lateral discharge ( $Rq_0$  decreases up to 3%). Such influence of  
358 the location of the obstacles on the modifications of discharge distribution should be considered in flooded  
359 urban areas for car park planning. Moreover, for a given obstacle, as the Froude number of the inflow  
360 increases, the impact of the obstacle strongly increases. Oppositely, it appeared that the water depth in the  
361 intersection has very limited influence on the impact of obstacles.

362 - For a given flow in which an obstacle is introduced, the impact on the discharge distribution is a  
363 direct consequence of the modifications of the following flow structures: i) streamwise and centrifugal flow  
364 acceleration, ii) width of the recirculation zone and iii) wake downstream the obstacle.

365 - Overall, the impact of the obstacles remains limited to about 10 to 15% of the inflow discharge even  
366 for very high Froude number flows. However, considering a scale ratio of about 25 between the experimental  
367 set-up and a real street (leading to a 7.5m wide street) and using a Froude similarity, the equivalent velocity  
368 would reach 1 to 2 m/s and the Reynolds number  $2 \times 10^6$  to  $8 \times 10^6$ . Assuming a typical street roughness height  
369 of 5 mm, the flow regime at the street scale will be hydraulically rough which may introduce some  
370 discrepancies when transferring the present results to real urban flood cases. Moreover, this impact is  
371 expected to increase with the size of obstacles, which is not covered in the present study. For flooding  
372 consideration, 10% to 15% change can be substantial. It is recommended to include these singularities as  
373 impervious areas within the topography of a city in 3D or 2D urban flood simulation or by a calibrated head  
374 loss term in 1D network simulation.

375

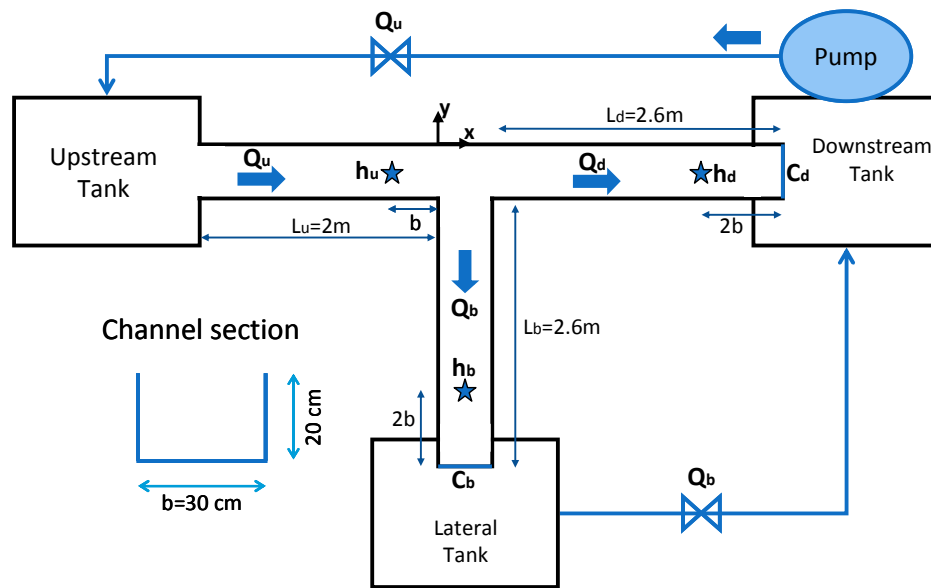
## 376 **5. Acknowledgements**

377 The work was supported by a grant from the PROCORE-France/Hong Kong Joint Research Scheme  
378 sponsored by the Research Grants Council and the Consulate General of France in Hong Kong (2011, project  
379 n°24664RB) and benefited from the support of the French CNRS, INSU, through grant EC2CO Cytrix 2011-  
380 231.

## 381 **6. References**

382 Barkdoll, B.D., 1997. Sediment control at lateral diversions, PhD dissertation, Civil and Environmental  
383 Engineering, University of Iowa, Iowa City, Iowa.  
384 Bazin, P.H., Bessette, A., Mignot, E., Paquier, A., Riviere, N., 2012. Influence of detailed topography when  
385 modeling flows in street junction during urban flooding. Journal of Disaster Research, 7 (5), 560-566.

- 386 Chen, D., Jirka, G.H., 1995. Experimental study of plane turbulent wakes in shallow water layer. Fluid  
387 Dynamics Res. 16 (1), 11-41.
- 388 Li, C.W., Zeng, C., 2009. 3D Numerical modelling of flow divisions at open channel junctions with or  
389 without vegetation, *Advances In Water Resources*, 32, 1, 49-60.
- 390 Li, C.W., Zeng, C., 2010. Flow division at a channel crossing with subcritical or supercritical flow. *Intern. J.*  
391 *for Num. Methods in Fluids*. 62, 56-73.
- 392 Lin, P., Li, C.W., 2002. A sigma-coordinate three-dimensional numerical model for surface wave  
393 propagation. *International Intern. J. for Num. Methods in Fluids*. 38, 1045-1068.
- 394 Mignot, E., Paquier, A., Ishigaki, T., 2006. Comparison of numerical and experimental simulations of a flood  
395 in a dense urban area. *Water Science and Tech*. 54, 65–73.
- 396 Mignot, E., Riviere, N., Perkins, R.J., Paquier, A., 2008. Flow patterns in a four branches junction with  
397 supercritical flow. *J. Hydr. Eng*. 134(6), 701–713.
- 398 Neary, V.S., Sotiropoulos, F., Odgaard, A.J., 1999. Three-dimensional numerical model of lateral-intake  
399 inflows. *J. Hydr. Eng*. 125(2), 126–140.
- 400 Ramamurthy, A.S., Tran, D.M., Carballada, L.B., 1990. Dividing flow in open channels. *J. Hydr. Eng*.  
401 116(3), 449–455.
- 402 Rivière, N., Perkins, R.J., Chocat, B., Lecus, A., 2006. Flooding flows in city crossroads: 1D modelling and  
403 prediction. *Water Science and Techn*. 54(6-7), 75–82.
- 404 Riviere, N., Travin, G., Perkins, R.J., 2007. Transcritical flows in open channel in tersections. 32<sup>nd</sup> IAHR  
405 Congress, 1-6 July 2007, Venice, Italy.
- 406 Riviere, N., Travin, G., Perkins, R.J., 2011. Subcritical open channel flows in four branch intersections.  
407 *Water Resources. Res*. 47, W10517.
- 408

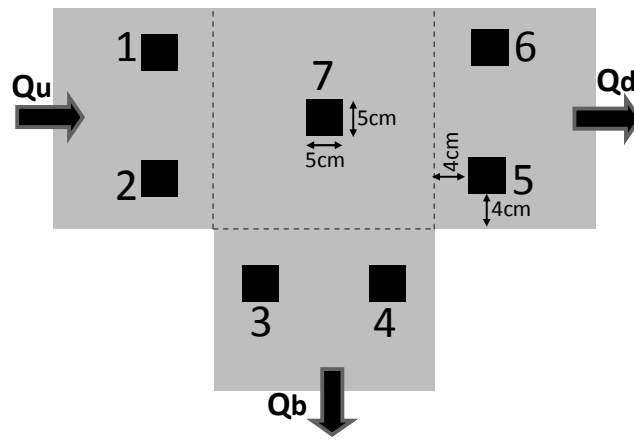


409

410

411

Figure 1: Scheme of the experimental set-up.



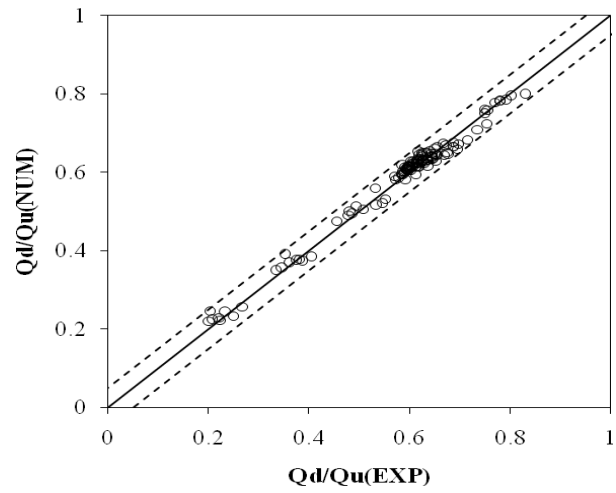
412

413

414

415

Figure 2: Location of the obstacles around the bifurcation.



416

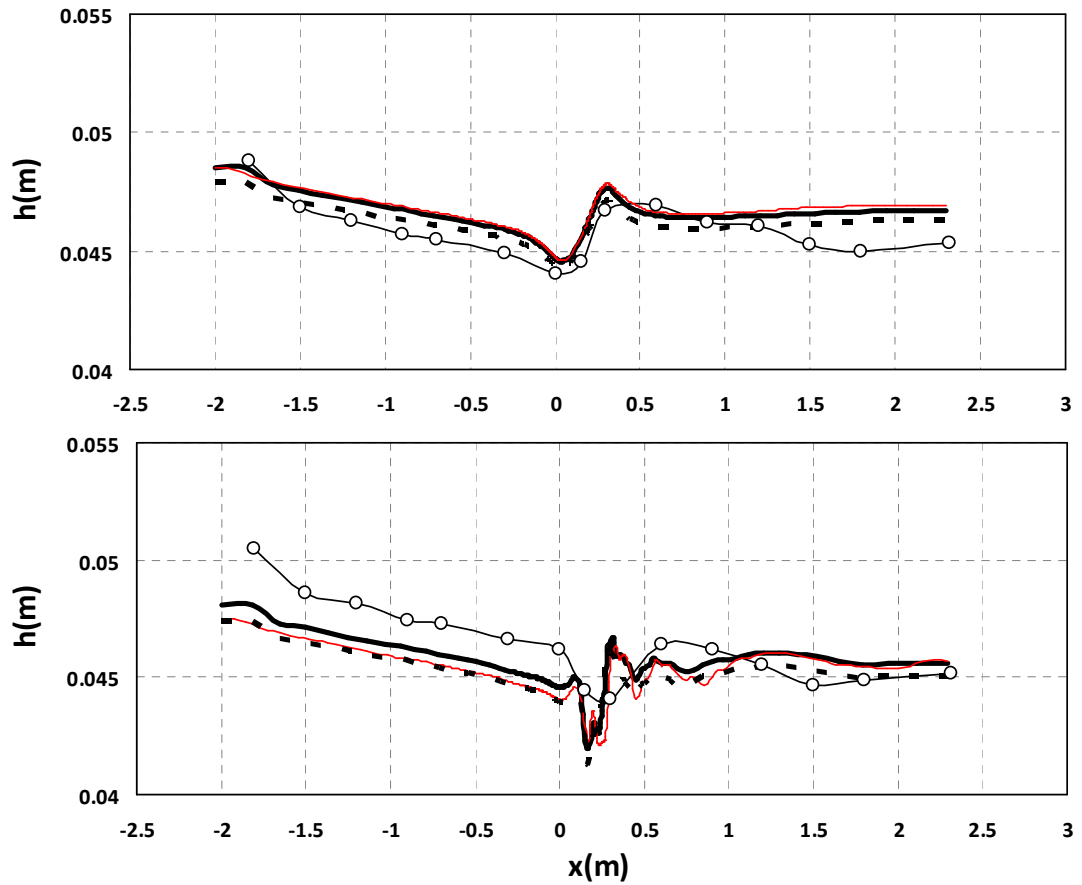
417

418

419

Figure 3: Comparison between measured (M) and computed (C) discharge ratios for the 14 flow x 10  
obstacle configurations. Dotted lines refer to  $\pm 5\%$  of  $Q_u$

420



421

422

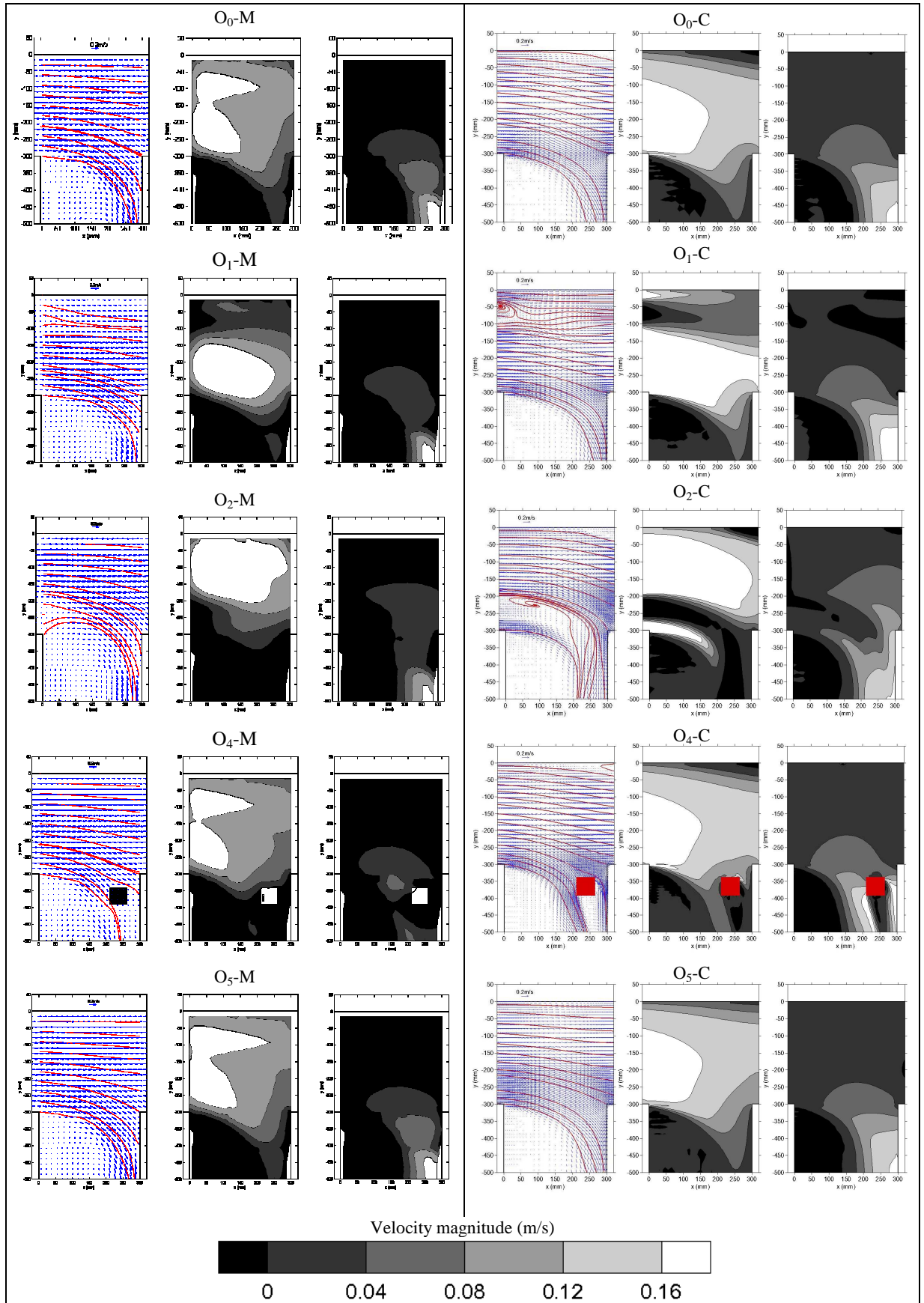
423

424

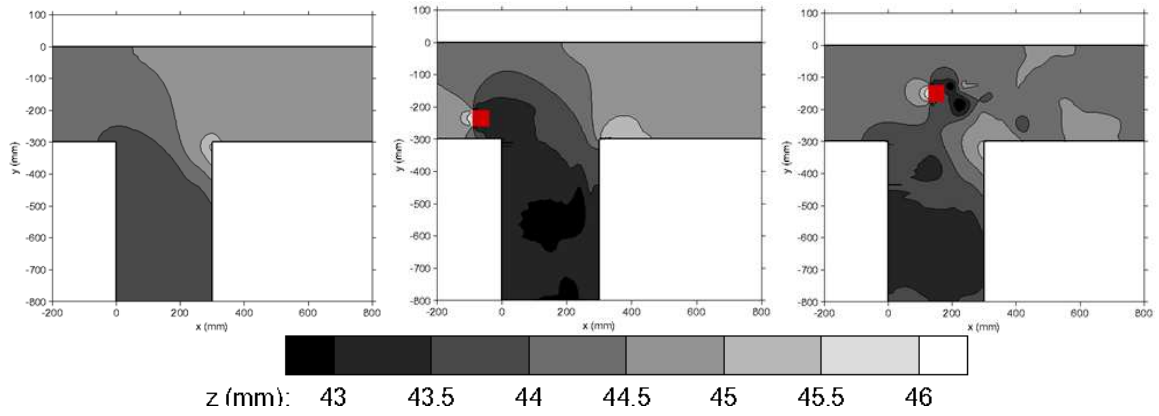
425

426

Figure 4: Measured (symbols) and computed backwater curves for the reference flow configuration (\* in Table 1) along the main channel at  $y=-0.22$ m without obstacle (O0, top) and with obstacle 7 (O7, bottom) using the reference numerical configuration (plain thick line), the refined mesh (red line) and the reference configuration with log profile at the inlet (dotted line).



430 Figure 5: Measured (M) and Computed (C) velocity fields at  $z=3\text{cm}$  for bold flow in Table 1 without obstacle  
431 ( $O_0$ ) and with obstacle configurations 1, 2, 4, 5. For each flow: left graph = velocity field with streamlines;  
432 center graph =  $u$  time-averaged velocity (along  $x$  axis); right graph =  $v$  time-averaged velocity (along  $y$  axis).  
433



434

435

436

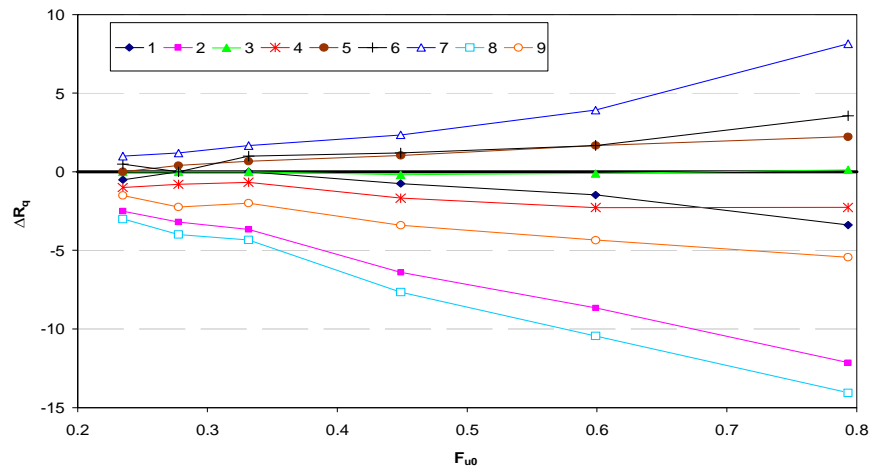
437

Figure 6: Computed free-surface elevation fields for bold flow in Table 1 without obstacle (O0) and with

438

obstacles O2 and O7.

439



440

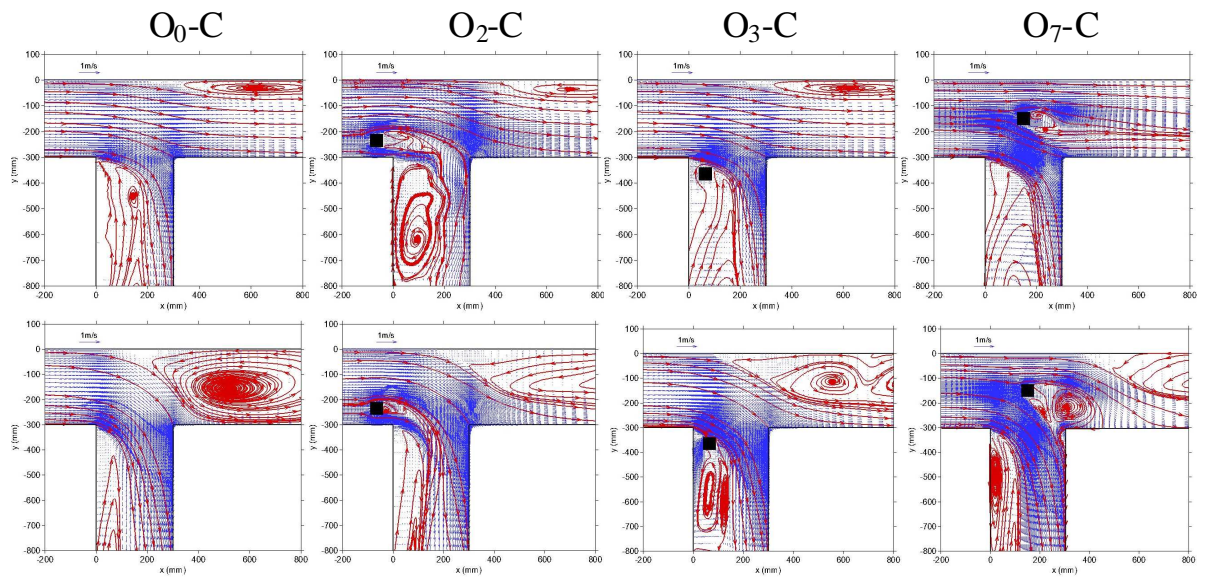
441

Figure 7: Measured impact of obstacles on the discharge distribution for flows in Serie 1 from Table 1 with

442

varying base upstream Froude numbers  $F_{u0}$ .

443



444

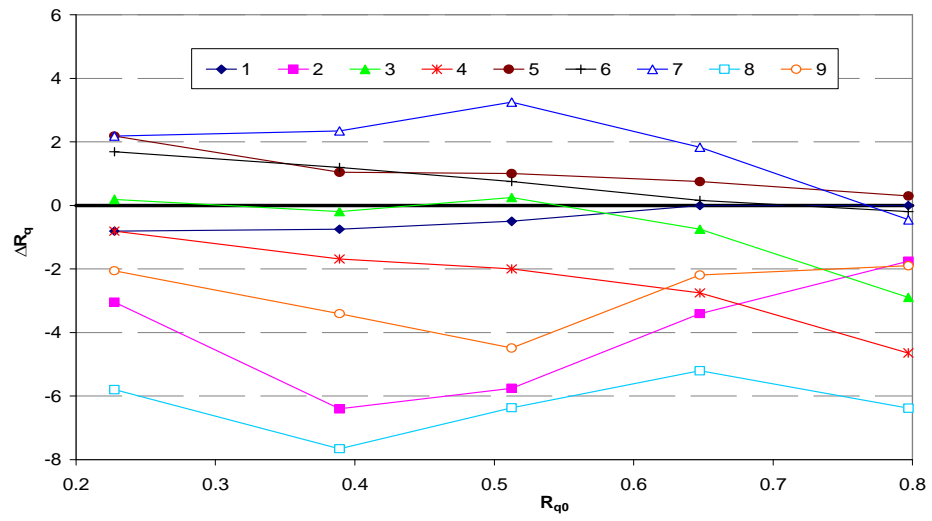
445 Figure 8: Computed velocity fields at  $z=3\text{cm}$  with obstacle configurations 0, 2, 3 and 7 for  $R_{q0}=0.39$  (top) and

446

$R_{q0}=0.8$  (bottom) in Serie 2 from Table 1.

447

448



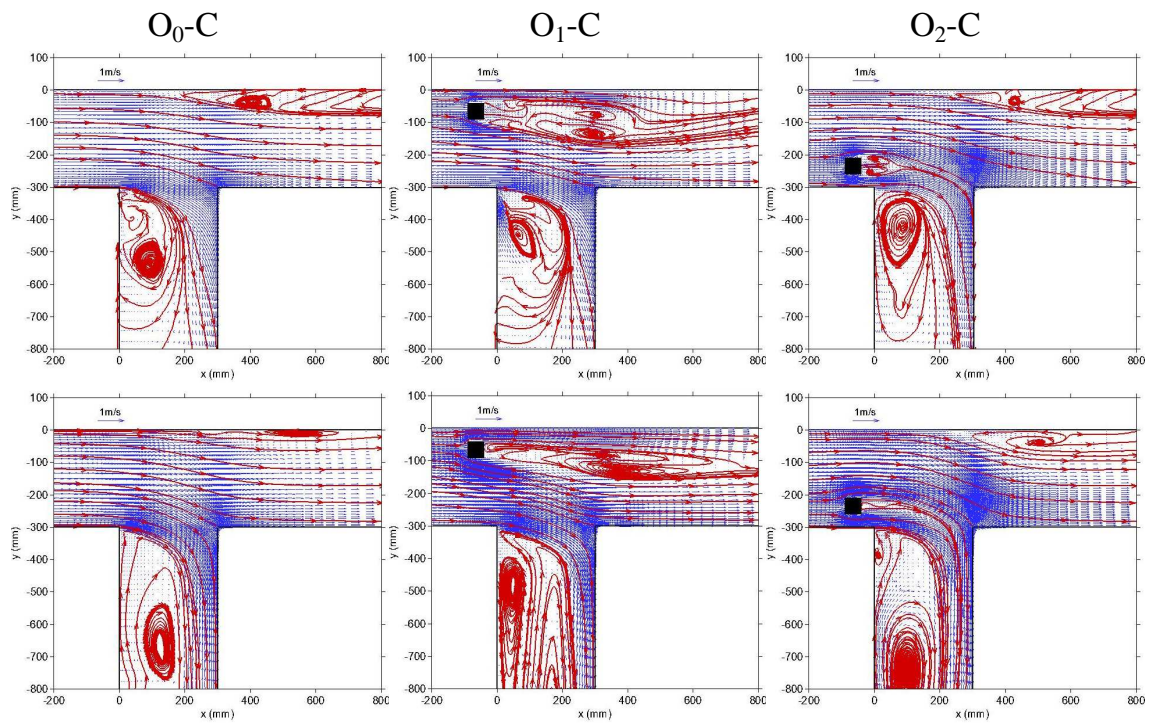
449

450

451

452

Figure 9: Measured impact of obstacles on the discharge distribution for flows in Serie 2 from Table 1 with varying base discharge distribution  $R_{q0}$



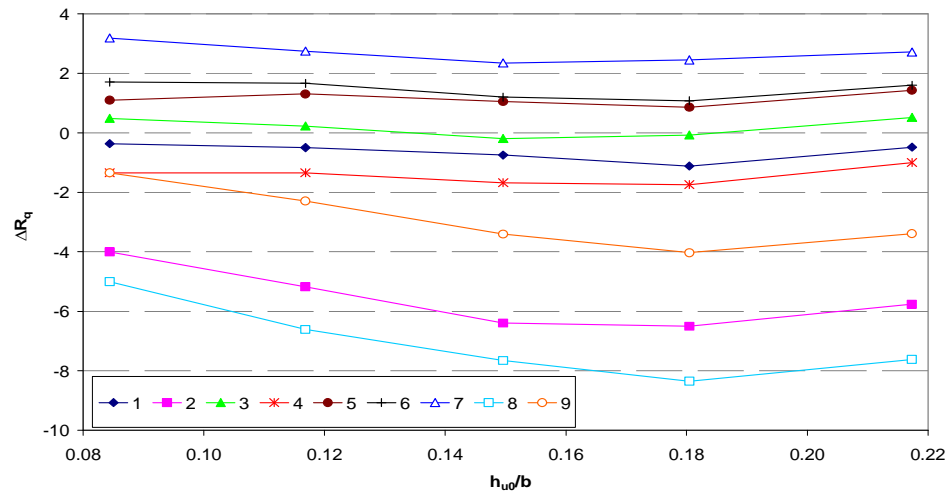
453

454 Figure 10: Computed velocity fields with obstacle configurations 0, 1 and 2 for  $h_{u0}/b=0.08$  (top) and

455

$h_{u0}/b=0.22$  (bottom) in Serie 3 from Table 1.

456



457

458

Figure 11: Measured impact of obstacles on the discharge distribution for flows in Serie 3 from Table 1 with

459

varying base upstream water depths  $h_{u0}/b$

460

461 Table 1: Non-dimensional parameters of the 14 flow configurations. The flow marked with an asterisk \*  
 462 (common to the three series) is referred to as the “reference configuration”. The first flow in bold, selected  
 463 for velocity field measurement, is referred to as “PIV measured flow”.

Serie #	$R_{u0}$	$F_{u0}$	$h_{u0}/b$
	<b>0.38</b>	<b>0.23</b>	<b>0.14</b>
	0.40	0.28	0.15
S1	0.39	0.33	0.15
	0.39*	0.45*	0.15*
	0.39	0.60	0.14
	0.39	0.79	0.13
	0.23	0.44	0.15
S2	0.39*	0.45*	0.15*
	0.51	0.45	0.15
	0.65	0.44	0.15
	0.80	0.45	0.15
	0.40	0.44	0.08
S3	0.38	0.45	0.12
	0.39*	0.45*	0.15*
	0.39	0.45	0.18
	0.39	0.45	0.22

464

465

466 Table 2 Grid refinement study of discharge distribution for the reference flow configuration (\* in Table 1).

No obstacle	$Q_u$ (L/s)	$R_q$	$h_u$ (mm)	$h_d$ (mm)	$h_b$ (mm)
Original	4	0.355	45.9	47.7	44.6
Fine grid	4.02	0.353	45.9	47.7	43.7

467

468

469 Table 3: Evolution of  $\Delta R_q$  as  $R_{q0}$  increases (Serie S2)

Obstacle #	Low $R_{q0}$ : sign of $\Delta R_q$ (Fig.8)	Evolution of $\Delta R_q$ as $R_{q0} \uparrow$ (Fig.10)
1	$< \mathbf{0}$	$\rightarrow \mathbf{0}$
2	$< \mathbf{0}$	$\rightarrow \mathbf{0}$
3	$\approx \mathbf{0}$	$\Delta R_{q3} < \mathbf{0}$
4	$< \mathbf{0}$	$\Delta R_{q4} \ll \mathbf{0}$
5-6	$> \mathbf{0}$	$\rightarrow \mathbf{0}$
7	$> \mathbf{0}$	$\rightarrow \mathbf{0}^*$
8	$< \mathbf{0}$	$\approx$
9	$< \mathbf{0}$	$\rightarrow \mathbf{0}$

470 \* $\Delta R_{q7}$  becomes negative for  $R_{q0} \geq 0.8$